optica

Electrically controlled waveguide polariton laser

D. G. Suárez-Forero,[1] ![ORCID] F. Riminucci,[2,3] ![ORCID] V. Ardizzone,[1,*] M. De Giorgi,[1] L. Dominici,[1] ![ORCID]
F. Todisco,[1] G. Lerario,[1] L. N. Pfeiffer,[4] G. Gigli,[2] D. Ballarini,[1] and D. Sanvitto[1,5]

[1]*CNR NANOTEC, Institute of Nanotechnology, Via Monteroni, Lecce 73100, Italy*
[2]*Dipartimento di Matematica e Fisica, "Ennio de Giorgi," Università del Salento, Campus Ecotekne, via Monteroni, Lecce 73100, Italy*
[3]*Molecular Foundry, Lawrence Berkeley National Laboratory, One Cyclotron Road, Berkeley, California 94720, USA*
[4]*PRISM, Princeton Institute for the Science and Technology of Materials, Princeton University, Princeton, New Jersey 08540, USA*
[5]*e-mail: daniele.sanvitto@nanotec.cnr.it*
Corresponding author: v.ardizzone85@gmail.com

Exciton–polaritons are mixed light–matter particles offering a versatile solid state platform to study many-body physical effects. In this work, we demonstrate an electrically controlled polariton laser, in a compact, easy-to-fabricate and integrable configuration, based on a semiconductor waveguide. Interestingly, we show that polariton lasing can be achieved in a system without a global minimum in the polariton energy-momentum dispersion. The cavity modes for the laser emission are obtained by adding couples of specifically designed diffraction gratings on top of the planar waveguide, forming an in-plane Fabry–Perot cavity. It is due to the waveguide geometry that we can apply a transverse electric field to finely tune the laser energy and quality factor of the cavity modes. Remarkably, we exploit the system sensitivity to the applied electric field to achieve an electrically controlled population of coherent polaritons. The precise control that can be reached with the manipulation of the grating properties and of the electric field provides strong advantages to this device in terms of miniaturization and integrability, two main features for the future development of coherent sources for polaritonic technologies.   © 2020 Optical Society of America under the terms of the OSA Open Access Publishing Agreement

https://doi.org/10.1364/OPTICA.403558

1. INTRODUCTION

A semiconductor system in which a photon emitted from an active medium has a larger probability of being reabsorbed than that of escaping out of the optical resonator is said to be in strong coupling. This condition accounts for the formation of the so-called exciton polariton: a light–matter quasi-particle resulting from the hybridization between an electromagnetic cavity mode and an exciton dipole in a semiconductor [1]. Since the first observation [2], polaritonic systems have become a suitable platform to study fundamental physical phenomena; effects such as optical parametric oscillations [3], bistability [4], Bose–Einstein condensation [5,6], superfluidity [7,8] and quantum vorticity [9] are some of the most intriguing phenomena that have been demonstrated. Peculiar features of polaritons such as long coherence time and high nonlinearities are chased for the realization of integrated optical elements [10]. Experimental devices such as polariton transistors [11] and routers [12] have indeed shown their viability for all-optical logic systems. More recently, the generation and manipulation of polaritons at the single or few particles level, have been reported, in an effort to assess the potential of these systems as a platform for quantum information processing.

The so-called "polariton condensate" [13] is one of the most paradigmatic effects observed in strongly coupled systems. This phenomenon is observed when a phase transition to a coherent state of polaritons takes place above a critical density, without any

population inversion. It has been demonstrated in systems such as semiconductor, organic, or hybrid microcavities [14–21] and photonic crystal cavities [22–24]. On the contrary, if the system undergoes the transition to the weak coupling regime before the condensate is formed, upon increasing power, a standard lasing effect starts to kick off. Optical waveguides (WGs) represent a very attractive platform for the exploitation of such coherent effects in actual devices, due to easy technological fabrication, the high quality factors achievable, and the particular geometry, suitable for the integration of polaritonic optical circuits and coherent optical sources. A guided electromagnetic mode, localized in the two-dimensional plane of the WG by total internal reflection, couples to an exciton confined to the quantum well (QW), giving rise to WG polariton modes [25,26], in counterposition to the more renowned microcavity polariton modes [1]. Recently, new WG designs have enabled the application of a transverse electric (TE) field, while keeping the system in the strong coupling regime [25,27]. In this work, we indeed show that, despite the lack of an energy minimum in the WG polariton dispersion, an electrically controlled polariton lasing effect can be achieved with guided polaritons propagating at high speed due to a spatially localized population inversion. It is worth nothing that here we use the terminology "polariton lasing" to distinguish this effect, a mixture between lasing under weak coupling and injection into a polariton mode, from the phenomenon of polariton condensation.

We use two metal gratings placed on top of a GaAS/AlGaAs slab that behave like a couple of semi-reflective mirrors, confining the WG polariton mode and outcoupling the laser emission vertically throughout one of their diffraction orders. Their design favors the formation of an energy gap in the energy momentum dispersion of the planar WG mode. Inside this energy interval, a manifold of Fabry–Perot (FP) modes is formed by the cavity effect between the gratings, funneling the light absorbed and reemitted by carrier recombinations under the pump spot. The lasing effect is then enabled on a specific polariton mode, i.e., the first mode for which gain equals losses upon increasing pump power. Parameters such as grating periodicity and filling factor as well as the cavity length (i.e., distance between gratings) provide a fine control of the laser properties, without the need for complex postprocessing of the WG. Most importantly, using an electric field applied in the direction perpendicular to the WG plane, we demonstrate real-time tunability of the emission wavelength. We stress that this electrical control is possible only because of the WG geometry, which allows to place the electrodes in close vicinity to the QWs, as has been previously reported on the same structure [25,27,28]. The strong coupling regime and the sensitivity of the exciton to the externally applied electric field allow us to obtain an electrically controlled polariton laser. These findings could be an important tool for the future development of polariton circuits, enabling the realization of a coherent source of propagating polaritons (if only a fraction of the polaritons in the lasing mode is extracted by the gratings), Q-switching, electro-optic modulators, and configurable logic gates.

2. RESULTS

The WG structure is grown on an n^+-doped GaAs substrate, on top of which a 500 nm cladding of $Al_{0.8}Ga_{0.2}As$ was previously deposited [25,27,28]. The structure consists of 12 pairs of 20 nm thick GaAs QWs separated by 20 nm of $Al_{0.4}Ga_{0.6}As$ barriers. Light is extracted through gold gratings spaced by a distance ranging from 50 μm to 150 μm. To realize FP resonators inside the WG, two identical gratings are fabricated facing each other on top of the slab at a given distance along their line of sight. A sketch of the full system is shown in Fig. 1(a), and the calculated spatial distribution of the electric field in-plane component is depicted in Fig. 1(b). We use gratings with pitch ~240 nm and filling factor of between ~0.72 and ~0.85. Finally, a 50 nm layer of indium tin oxide (ITO) is sputtered on top of the sample. This layer, together with the doped substrate on the opposite side, allows for the application of an electric field in a direction perpendicular to the slab plane. The purpose of the electric field is to tune the exciton energy, exploiting the Stark effect, and hence its influence on the polaritonic guided modes [25,27,28]. A more detailed description of the structure is given in Section 4.

To first verify the presence and features of the WG modes inside the slab, we use a nonresonant pump laser that excites the sample outside of the gratings region, while the photoluminescence (PL) spectrum of the system is collected through an individual grating (so no cavity is formed) placed 100 μm away from the off-resonant excitation spot. Figures 1(c) and 1(d) show the PL emission coming from the hybridized zeroth-order transverse magnetic TM and TE modes of the structure, respectively. The dispersions are plotted as a function of the wavevector β of the propagating mode inside the slab. The uncoupled bare exciton line (heavy hole exciton) and guided optical modes are indicated by horizontal and oblique red
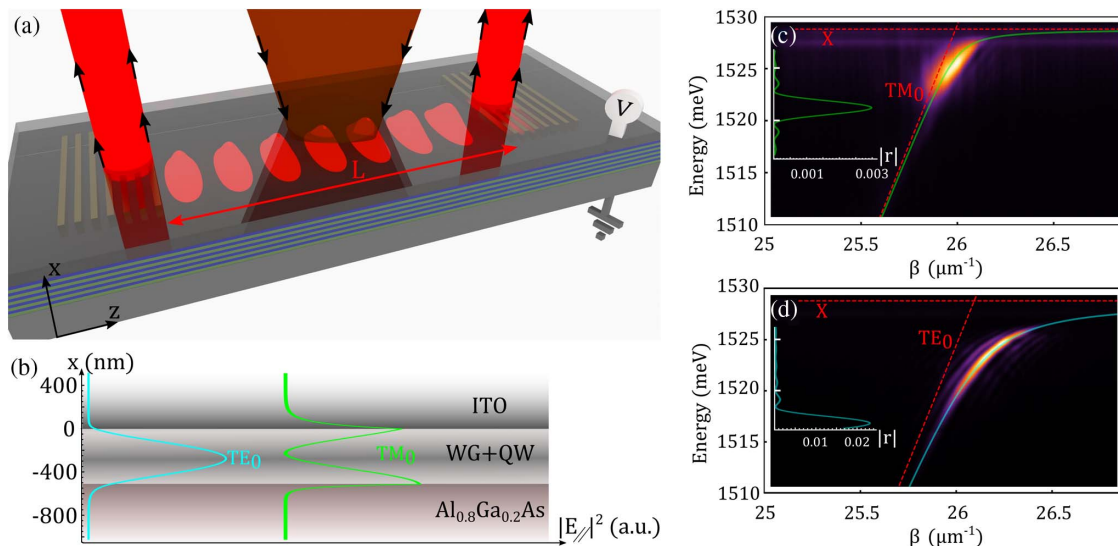

Fig. 1. (a) Schematic representation of the system. Two gold gratings, placed on top of the WG, couple to the vanishing tail of the guided modes. As a result, a FP cavity is formed inside the slab for the TM mode, opening the possibility to observe a lasing effect in the system. L is the cavity length given by the distance between the gratings. The doped substrate, together with a top layer of ITO, enables the application of an electric field in the direction perpendicular to the cavity plane. (b) Calculated intensity profile of the in-plane electric field for each guided mode. The x component of the electric field for the TM_0 mode is not included in the scheme because it does not contribute to the light–matter coupling. (c), (d) Polarization resolved PL dispersion of the system extracted through a single gold grating placed on top of the slab WG. Each dispersion is plotted as a function of the wavevector of the guided modes β. Panel (c) corresponds to TM polarization, while (d) shows the dispersion for the TE mode. Continuous lines correspond to a fitting of each mode by using a theoretical model of coupled oscillators. The obtained Rabi splitting (Ω) values are 5.2 meV for TM mode and 13.4 meV for TE. The bare exciton and photonic modes are indicated by red dashed lines. The calculated reflectivity of the mode in the presence of the grating is displayed as an inset for each polarization. The creation of reflectivity maxima indicates the opening of energy gaps.

dashed lines, respectively. The experimental polariton dispersion can be fitted by means of a theoretical model of coupled oscillators, as shown by the solid lines in Figs. 1(c) and 1(d). The results show an asymmetry in the Rabi splitting (Ω) between TE and TM modes. We obtain values of 13.4 meV and 5.2 meV, respectively. As a matter of fact, this is predicted by the selection rules for the coupling of the confined modes with the exciton dipole, which imply an Ω value around three times higher for the TE mode than for the TM mode, as has already been observed in similar samples [25,29]. The figure also evidences an important difference in the resolution in β with which the TE and TM modes are outcoupled. This linewidth effect is originated by the different grating efficiencies with respect to each polarization, and it is correlated with the formation of the FP cavity inside the structure, as will be described in detail in the Section 3.

After the WG modes, we also characterize the features of the top gratings and their role in forming the FP cavity. Figure 2(a) shows the angle-integrated PL emission intensity from the terminal end of a single and very extended, 400 μm long grating as a function of the emission energy. Both TE and TM polarizations possess a local minimum in the emitted intensities, highlighted by vertical arrows in the figure. These minima represent energy gaps corresponding to wavevectors of the guided modes that are back-reflected by the grating. In other words, each grating acts as a mirror in the energy interval corresponding to the gaps in Fig. 2(a), and when two gratings face each other, a planar FP cavity is formed, with a cavity length that depends on the distance L between gratings. The cavity modes are characterized now due to the PL emission outcoupled from one of the gratings when a nonresonant pumping spot is placed in the middle between the two, as illustrated in Fig. 1(a). Figure 2(b) shows the PL emission of the cavity modes formed along the TM_0 mode by placing the gratings at distances of $L = 50$ μm (black upper line), $L = 100$ μm (middle blue line),

and $L = 150$ μm (lower red line). As expected, the closer the gratings to each other, the larger the free spectral range. In the case of the gratings separated by 50 μm, the mode spacing is ∼2.3 meV, which corresponds to the FP mode of manifold 17. For the case of a pair of gratings separated by 100 μm, the spacing is ∼1.4 meV (manifold 30), and for the gratings separated by 150 μm, the spacing is ∼0.9 meV (manifold 45). Our system, then, is not operating near the global energy minimum, which would occur at the smallest guided wavevector (i.e., at much smaller energy and for a negligible excitonic fraction). It operates instead at the local minima of the FP modes, i.e., at the bottom of the parabolic dispersion of each FP mode. The observed FP modes are, then, an effect of the confinement of the TM_0 mode due to the presence of two identical gratings. A comparative analysis of the extracted PL is performed with respect to the fabrication and materials features of the grating(s) (Fig. S4) and shows that when the metallic grating is in direct contact with the dielectric guide, it carries a considerable spectral broadening of the measured TM mode (and not of the TE one). We assign this broadening to an additional residual absorption from plasmonic modes in the gold grating, a widely studied effect [30–32]. It is important to note that this possible plasmon induced absorption takes place only in the grating region and does not modify the truly WG polariton character of the propagating modes outside the gratings, as demonstrated in Fig. S4(c), where the PL emission collected through a fully dielectric grating confirms the expected behavior for a system operating in the strong coupling regime. For an extended discussion with respect to the grating features, we refer the reader to Supplement 1.

We have characterized all three building blocks (namely, the WG modes, gratings, and planar FP cavity), which are mandatory for the observation of the waveguiding lasing effect. We can hence shine a high-peak-power nonresonant laser in a region between the two gratings; specifically, we use a 100 fs pulsed laser tuned at 1.59 eV (≈780 nm) and 80 MHz repetition rate, with a spot size of 40 μm. Figure 3(a) shows the PL emission in real space at threshold excitation power. The big spot between the gratings corresponds to the exciton emission under the pump spot that is not coupled to the guided modes. The excited guided polariton modes propagate along the slab with in-plane vector β and are partly extracted and partly reflected back in the plane when they hit the gratings, highlighted by white rectangles. The PL emission extracted from grating 1 can be resolved in both energy and momentum [Fig. 3(b)]. Remarkably, such emission shows a series of discrete peaks along the TM polariton dispersion corresponding to the FP modes in Fig. 2(b). In other words, in the region of space between the two identical gratings, a FP cavity is formed, sustaining the discrete modes observed in Fig. 3(b). With increasing pump power, as shown in Figs. 3(c) and 3(d), the system shows a clear threshold behavior [see inset in (d)] with prominent coherent emission from only one of the FP modes at an energy of ∼1520.5 meV, which in the dispersion relation corresponds to a wavevector $\beta = 25.96$ μm^{-1}. This is the precise in-plane wavelength corresponding to the grating pitch Λ, where it is hence maximally reflective. A strong reduction of the FP mode linewidth is observed across the lasing threshold [Fig. S5(a)]. Moreover, when the emitted light from the two gratings is overlapped in k space, an interference pattern is generated [see Figs. S5(b)–(g) for the build-up of the first-order coherence across the lasing threshold]. The threshold and linewidth effects are clear signatures that mark the onset of the lasing regime in the system.
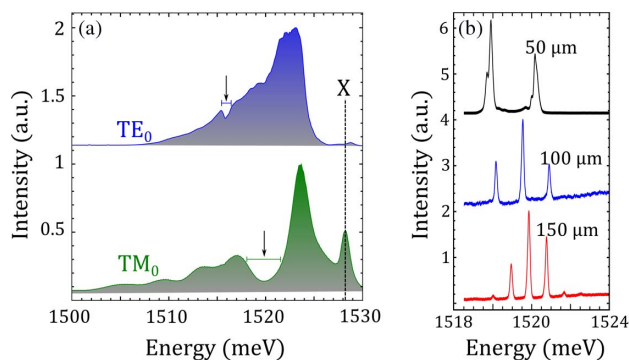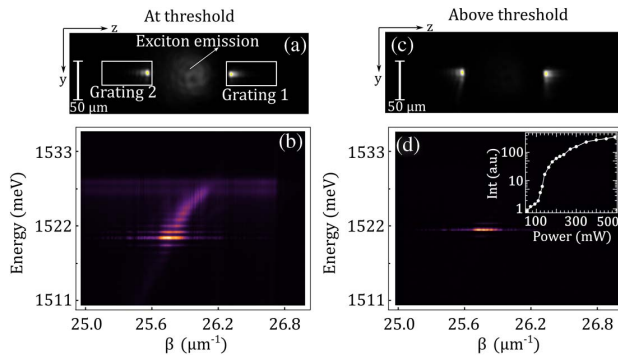

Fig. 2. (a) Experimental measurement of the gratings gap in TE and TM polarizations. The spectra are obtained by integrating the PL emission from the terminal end of a 400 μm long gold grating over the emission angle. The vertical dashed line indicates the exciton energy. The opening of two bandgaps is highlighted by the vertical arrows. (b) Fabry–Perot modes formed along the TM_0 dispersion. The constructed FP cavities have different lengths, determined by the distance between the gratings. As expected for an optical cavity, the smaller the cavity, the greater the free spectral range at a given energy. The spectral distances of 2.3 meV for the cavity of length 50 μm, 1.4 meV for the cavity of 100 μm, and 0.9 meV for the cavity of 150 μm, are associated with FP modes of manifold 17, 30, and 45, respectively. In the three cases, the system is pumped near the threshold power (110 mW, 110 mW, and 150 mW, respectively.), where the FP modes become visible, and the spot is placed at the center of the FP cavity.

Fig. 3. (a) Real space image of the 100 µm long FP cavity when excited out of resonance near the threshold power (95 mW). The laser spot is placed in the middle of the cavity, exciting both the QW exciton with low in-plane momentum (central spot) and the polaritonic guided modes, extracted from the gratings (white rectangles). The residual pump laser signal is suppressed with a long-pass spectral filter. (b) The TM mode is reconstructed in the Fourier space by spatially isolating the PL from grating 1. The insertion of the gratings entails an additional confinement, and hence the formation of discrete modes along the TM dispersion, as can be observed in the image. (c) When the pump power overcomes the threshold (140 mW), one mode of the cavity gets massively populated, reaching an emission intensity much higher than any other emission in the system. (d) The PL dispersion measurement [measured as in (b)] confirms which state of the FP cavity gets populated. The inset in (d) shows the intensity of the lasing mode as a function of the pumping power; a clear threshold behavior is visible.

Finally, we can now apply an external electric field perpendicular to the plane of the slab, demonstrating an extra degree of freedom acting as an additional control parameter on the WG

polariton lasing. Figure 4(a) shows the spectra obtained from the TM polariton dispersion at $\beta \approx 26$ µm^{-1} and for different applied voltages. The TM dispersion is modified due to the Stark effect that red shifts the exciton energy. In Figs. 4(b) and 4(c), we measure the central emission energy and the linewidth of the lasing mode for three different applied voltages and as a function of the pump power. For small applied fields (≤ 0.9 V), a red shift of the lasing mode is observed. When the applied electric field is further increased (>0.9 V), the exciton energy approaches the cavity modes, more greatly altering their absorption properties, and hence, their relative losses. As a matter of fact, Fig. 4(d) shows that for an applied voltage of 1.5 V, the mode in which the stimulated emission takes place jumps to the next manifold (both spectra are taken at threshold power). The electric field acts in this case as a neat switch that allows to select the mode in which the lasing takes place by modifying the FP modes' relative losses. The inset of Fig. 4(d) shows the evolution of the linewidths of the two lasing peaks upon application of the electric field. Indeed, the switch between the lasing modes also coincides with the crossing of their linewidths. We can access the temporal dynamics of the process by means of a streak camera coupled to a monochromator and a scan in the reciprocal space. The energy-momentum dispersion resolved at different times is shown in Fig. 5 (see also Supplement 1, Visualization 1 and Visualization 2). In the case of Figs. 5(a)–5(c) the pump spot is placed between the two gratings, and the emission from only one of the gratings is recorded [see Fig. 5(d)]. Figure 5(a) shows the far-field emission 200 ps after the arrival of the pump pulse (at the lasing threshold power). The FP modes are clearly visible. These modes are in TM polarization, i.e., the polarization for which the two gold gratings act as mirrors. Even when the FP mode population fades away, Figs. 5(b) and 5(c), the TE mode (labeled
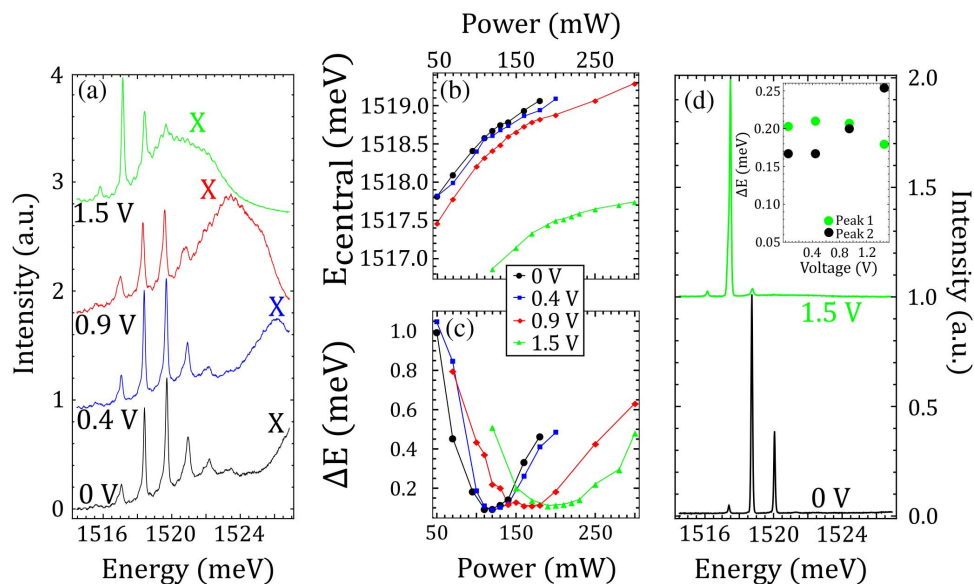

Fig. 4. (a) Spectra obtained from a profile of the TM polariton dispersion at $\beta \approx 26$ µm^{-1}, and for different applied voltages. The letter X indicates the peak corresponding to the PL emission of the uncoupled exciton that red shifts due to the Stark effect. (b), (c) To verify that the presence of a transverse electric field does not affect the properties of the lasing effect, we measure the (b) central energy shift and (c) spectral narrowing for three applied voltages. The results not only confirm the lasing effect in every case, but show that the electric field acts as a fine-tuning of the laser energy for small voltages, and as a switch that allows to select the cavity mode in which the lasing takes place. The latter effect is achieved as a consequence of a modification of the relative Q factor of the cavity modes, since the exciton resonance affects the absorption at the energy of each FP mode. (d) Spectra of the cavity taken at threshold power without any transverse electric field (black) and with an applied voltage of 1.5 V (blue). The modes' energy is almost unaltered, but the change of their absorption properties switches the mode in which the stimulated emission takes place. The inset shows the FWHM of each peak as the applied electric field increases. When the quality factor of peak 1 decreases below the one of peak 2, the lasing mode switches. The data are acquired in the FP cavity of 100 µm while pumped at the center. The emission is collected from one of the gratings in the far field.
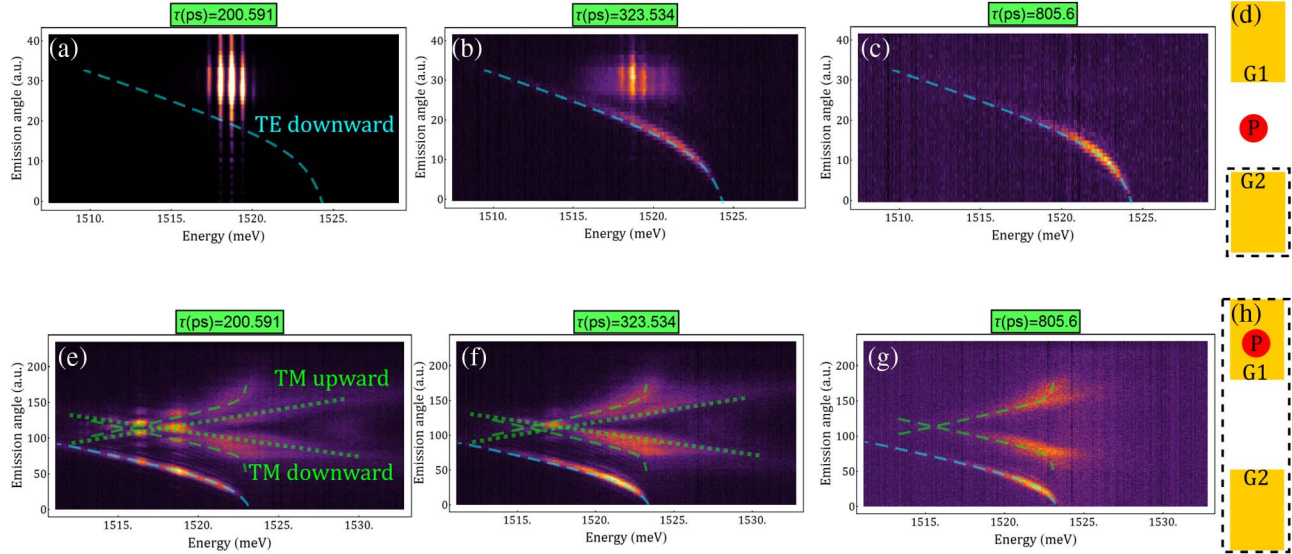
Fig. 5. Temporal dynamics of the system after the arrival of the pumping pulse. The upper panels correspond to the case in which the FP cavity is pumped at the center and the emission is collected from the lower grating [see sketch in (d)], while in the lower panels, the pumping laser is placed on the upper grating and the emission is collected from both gratings and overlapped in the Fourier plane [see sketch in (h)]. In each case, there is a visual guidance to identify the TE mode in the upper panel, and the coupled TE (dashed blue), TM (dashed green), and uncoupled TM (dotted green), in the lower panel. The cavity has a length of 100 µm and is pumped with a power of 95 mW. In (d) and (h), the red dot indicates the pump spot position and the yellow rectangles the metallic gratings. The dashed black line highlights the spatial region from which the emission is collected.

"TE downward") is still visible. Figures 5(e)–5(g) show the temporal dynamics when the pumping spot is placed on one of the two gratings, G1, and the far-field emission is collected from the whole cavity area [see sketch in Fig. 5(h)]. Again, after about 200 ps from the arrival of the pump pulse, we observe lasing emission from the TM modes [see Fig. 5(e)] (note the interference coming from the superposition of the light emitted from G1 and G2). Interestingly, the portion of the sample under the pumping spot (grating G1) shows both weak and strong coupling features [respectively, dotted and dashed dispersions in Figs. 5(e) and 5(f)], while the light coming from grating G2 shows strong coupling features (e.g., the TE mode propagating downward). Figures 5(f) and 5(g) show that as carriers recombine and weak coupling features are lost, the lasing emission fades away. These observations strongly suggest a connection between weak coupling under the pumping spot and the polariton lasing emission. We also note that in Figs. 5(e)–5(g), the TE mode propagating upward is not visible. We think that this is due to the fact that only a small portion of grating G1 is free from the pumping spot and able to extract the TE mode propagating upward (while the whole G2 contributes to the extraction of the downward propagating TE mode). Moreover, the extraction efficiency of the gratings is smaller for the TE modes than for the TM modes, which explains why the upward propagating TM mode is instead visible.

3. DISCUSSION

We demonstrated the design and realization of a micrometer-sized laser in a GaAs/AlGaAs polariton WG by using two metallic gratings at a controlled distance on top of the slab WG, in order to form a FP cavity that confines the photonic field in one dimension. To better understand this effect, we calculate the influence of the grating on the guided modes by using a perturbation formalism to study the coupling between counter-propagating modes [33,34].

For a WG grown in the x direction, and with modes propagating in the z direction, the magnetic field $H(x, z, t)$ of the mth TM mode, can be expressed in the case of an infinite slab in the y direction and neglecting any variation along the k_y direction as

$$H_m(x, z, t) = \mathcal{H}_y^m(x)e^{i(\omega t - \beta_m z)}, \tag{1}$$

where $\mathcal{H}(x)$ is derived from the corresponding wave equation and boundary conditions under the "long wavelength" approximation, which takes into account the internal WG periodicity (12 pairs of QW+barrier) by considering an effective refractive index. A numerical verification of the validity of this approach, upon comparison with a full transfer matrix method, is presented and discussed in Fig. S2 of Supplement 1, together with its detailed explanation, based on [35]. The fabrication of a grating with periodicity Λ on top of the WG acts as a perturbation that changes the effective in-plane momentum of the mth mode as

$$\beta'_m = \frac{l\pi}{\Lambda} - \sqrt{\left(\beta_m - \frac{l\pi}{\Lambda}\right)^2 - |\kappa|^2}, \tag{2}$$

with β_m the in-plane momentum of the unperturbed mth mode, l an integer number such as $|\beta_m - \frac{l\pi}{\Lambda}| \sim 0$, and κ a constant that depends on the grating periodicity and material, and the spatial profile of the transverse field. In the case of a square grating fabricated on top of the slab, with filling factor a, height h, and refractive index n_g, the constant κ takes the form

$$\kappa = \frac{i\omega\mu_o}{4\pi l}\text{Sin}(\pi la)\int_0^h \left(\left(n_g/n_{\text{ITO}}\right)^2 - 1\right)\left[\mathcal{H}_y^m(x)\right]^2 dx. \tag{3}$$

This expression indicates the existence of an energy gap in the guided mode dispersion in the region covered by the grating when $|\kappa|^2 > (\beta_m - \frac{l\pi}{\Lambda})^2$. At the energy interval around the exciton ($\sim$1.529 meV), where the electromagnetic field hybridizes,

the in-plane linear momentum of the TM guided mode lies in the range ($25.6\ \mu m^{-1} < \beta_m < 26.3\ \mu m^{-1}$), as observed in Fig. 1(c). For a grating with period $\Lambda = 243$ nm, the condition $\beta_m - \frac{l\pi}{\Lambda} \sim 0$ is satisfied for $l = 2$. Expression (3) shows that, for l even, κ differs from zero only for filling factors different from 0.5. Moreover, it is also evident from the expressions that for $l = 2$, the maximum gap's amplitude is obtained for a filling factor of either 0.25 or 0.75. In our case, we fabricated gold gratings with a filling factor close to 0.75 to maximize the coupling between propagating and counter-propagating modes and hence their reflectivity, whose calculation is shown on the left side of Figs. 1(c) and 1(d). The Purcell enhancement effect induced by the semi-reflective gratings provides the conditions for the lasing from the FP mode with energy $E \sim 1520.5$ meV and in-plane wavevector $\beta \sim 25.96\ \mu m^{-1}$ [Fig. 3(d)]. The theoretical dispersion fitting reveals that the excitonic fraction of the coherent polariton population is $|C_x|^2 = 0.1$ at 0 V. This value increases for an applied electric field, given that it only slightly modifies the position of the FP modes, while it strongly affects the polaritonic dispersion. In other words, while the excitonic resonance explicitly modifies the polariton dispersion, its tail produces only small changes in the FP modes. An attractive feature of this system is that the excitonic component of the generated coherent population can be tailored by engineering the parameters of the FP cavity, in particular, its length (distance between gratings) and the grating period. Hence, no modification of the slab WG is required.

It is worth noting that the blue shift in Fig. 4(b) cannot be associated simply with polariton–polariton interactions, since the exciton energy remains almost unaltered when the pump power is increased. It rather might depend on a local carrier induced reduction of the WG refractive index [36], due, for example, to the plasma generated by the optical pump pulse, i.e., a plasma induced transparency [37,38] or to the band filling effect. Such effects can be especially relevant in the spatial region below the pump spot. An estimation of the index change with increasing pump power can be done by considering that the ith mode of the resonator has energy $E_i = i \frac{h \cdot c}{2Ln}$, where L is the cavity length, given by the distance between the gratings, n its effective refractive index, h the Planck's constant, and c the vacuum light speed. The data show a saturation behavior compatible with such an explanation, with a reduction of only 10^{-4} in the refractive index. Figure 4(c) shows the linewidth for different pump powers and voltages. The observed spectral narrowing at threshold is expected, and it is associated with the fact that the coherence time of the system exceeds the radiative lifetime of the confined mode under these excitation conditions [14]. Based on the optical characterization of the system and the complex temporal dynamics that we observe in Fig. 5 (see also Supplement 1, Visualization 1 and Visualization 2), we can explain the laser build-up in the following way: the gain media (QWs) are populated through the nonresonant pump in the middle of the FP cavity, as shown in Fig. 3(a), forming an electronic plasma localized under the pumping spot. After the recombination of photo-created carriers, the photons can be emitted in any of these FP modes (as the Purcell factor enhances the emission in them). By following standard laser theory [39], the first mode to start to lase is the one for which a threshold condition is met. In the dynamics of our system, this condition is achieved after about 200 ps, as shown in Figs. 5(a) and 5(e). This condition is written in terms of the critical population inversion: $N_C = \gamma/\sigma L$, where N_C is the population at which the lasing starts, and σ is the spontaneous emission

coefficient. Here γ represents the overall losses of a given mode as $\gamma = -\ln(R_1) - \ln(R_2) - \ln(1 - L)$, in which R_1 and R_2 are the mirror reflectivity, and L represents the losses for a roundtrip in the cavity. The first mode to start to lase is then the mode with the smaller N_C, i.e., the mode with the smaller linewidth in the set of FP modes created by the two gratings. By modifying the linewidth of the modes, as shown in Fig. 4(d), it is possible to change the mode that starts to lase. It is important to remark that while the mechanism of the laser can be explained simply, the coherent population generated has an interactive nature, which could carry some complex effects of competition between modes, perhaps involving polariton nonlinearities. While these effects could be interesting, they are beyond the scope of the present work. An additional feature revealed by Figs. 5(e)–5(h) is the particular coexistence between populations in strong and weak coupling inside the FP cavity (see also Supplement 1, Visualization 2). The signal extracted from the upper grating (G1), shows a superposition of population in strong coupling (green dashed lines) and weak coupling (green dotted line). This population has a much longer lifetime than the FP modes, as can be observed in Fig. 5(f), where the coherent population has already left the cavity, but the coupled and uncoupled TM population is still present. While we detect complex emission patterns under the laser spot, which can be identified as carrier recombination in a weak coupling regime, the emission from G2 corresponds to a WG polaritonic dispersion in strong coupling. This evidence goes in the direction of the creation of an electronic plasma under the pump spot, i.e., to an inversion of population. However, this plasma is restricted exclusively to the illuminated region (since the excitonic group velocity is too low to provide significant propagation during the excitonic lifetime). The radiative decay of this population into the polaritonic guided mode of the FP cavity with the lowest losses enables the massive population of such a state, creating the coherent state of guided polaritons. The full process can then be interpreted as the coexistence of an electronic gas (in weak coupling) that preferably decays into a polaritonic guided mode, generating a coherent population of propagating hybrid light–matter particles (in strong coupling). The long lived exciton population keeps feeding the cavity modes during the full lasing process and after the emission of the coherent population, as observed in Figs. 5(c) and 5(g), a proof that the quality factor of the slab WG is much higher than the one of the FP cavity. The observation of the coupled TE mode (dashed blue line) during the full time range demonstrates the coexistence of dressed and bare states inside the cavity. We note also that recently a polariton laser effect has been claimed at both cryogenic and room temperature in ZnO-based WGs [40]. In that case, the polariton emission is interpreted as a standard polariton condensate without need for population inversion. While this interpretation can be supported by the large Rabi splitting observed in ZnO systems, our present work shows that in guided polariton systems, an alternative interpretation can explain the same features. Moreover, the absence of a blue shift in the case in [40] could also be compatible with a refractive index change in the region between the two cracks. A careful check of the dynamics both under and outside the pumping region is essential in this kind of system to better clarify the lasing mechanism involved.

It is also worth noting that electrical control of polariton properties such as plasmon–exciton coupling [41], spin switch [42], and parametric gain [43] have been reported. While the optimization and precise characterization of the electrical control presented here

is beyond the scope of this work, it is interesting to compare the theoretical minimum electric energy required for the switch in Fig. 4(d) with the value reported for the spin switch in [42]. To do this, we consider our heterostructure as a capacitor with capacity $C = 9 * 10^{-13}$ F/m. In an optimized version of the present device, electrodes having an area as low as 100 µm ∗ 150 µm would be enough to apply the electric field of 1 V required in Fig. 4(d). Under these hypotheses, the required switching energy would be on the order of 600 fJ. This value is about two orders of magnitude higher than the value reported in [42], which is probably due to the different physical mechanism involved: the spin state of the condensate is very sensitive to crystal birefringence and heavy-hole/light-hole mixing, and a small applied electric field is enough to achieve the spin switching. In our case, the mode switching is obtained by shifting the exciton energy by the Stark effect, requiring higher applied electric fields and an increased amount of energy.

In summary, we report a lasing effect providing a coherent population of high-speed, guided polaritons. The additional optical confinement necessary to achieve the laser emission is provided by placing two specifically designed gold gratings on top of the WG. It is worth to note that this design is versatile, easy to fabricate, and does not require complex post-processing of the WG, such as vertical selective etching. Most important, due to the WG geometry, we demonstrate an effective electrical control of the vertical laser emission. Remarkably, by electrically tuning the quality factor of the modes, we obtain an electrically switched polariton laser. This effect could be exploited for the realization of electrically Q-switched sources of polaritons. More generally, the lasing effect we report in this work would allow the construction of tunable, micrometer-sized coherent sources of polaritons with different properties in a single wafer of slab WG. We think that our findings could be valuable in polaritonics, especially in the development of polaritonic circuits and integrated polaritonic logic elements.

4. MATERIALS AND METHODS

WG sample. The full structure is grown on top of an n^+-doped GaAs substrate 500 µm thick. The cladding layer is made of 500 nm of $Al_{0.8}Ga_{0.2}As$, while the WG is composed of 12 bilayers of $Al_{0.4}Ga_{0.2}As$ barrier (20 nm thick) and GaAs QW (20 nm thick), and a final bilayer made of 20 nm of $Al_{0.4}Ga_{0.2}As$ and 10 nm of GaAs.

    Fabrication of gold gratings and deposition of ITO. To fabricate gold gratings onto the sample, we relied on a lift-off process. By design, they are 100 µm long, 50 µm wide, and have a pitch of 243 nm. Their production requires a positive e-beam resist PMMA A4 to be spun at 4000 rpm onto the sample and baked for 3 min at 180°C. The latter is then exposed using Raith150 and developed in MIBK:IPA 1:3. Subsequently, 3 nm of chromium and 30 nm of gold are thermally evaporated. The sample is placed in Remover PG at approximately 80°C to remove the resist. A SEM characterization of the obtained gratings is displayed and discussed in Supplement 1 (Fig. S3). The dense pattern carries irregularities in the first few grating wires related to the "proximity effect" [44], very common in electron beam lithography. As shown and discussed in Fig. S3, the affected area is negligible with respect to the full grating sizes. In closing, the electric contact is obtained by uniformly sputtering 50 nm of ITO on top of the sample; the gold grating results are completely covered in the end.

    Optical measurements. For all of the optical characterization, the sample is kept at a cryogenic temperature of 4 K.

All PL measurements are realized in a confocal configuration, using a 100 fs pulsed laser with a repetition rate of 80 MHz, tuned at 1.59 eV (≈780 nm) to excite the sample out of resonance. The detection system allows to reconstruct either real or Fourier spaces in a charge coupled device (CCD) coupled to a monochromator 70 cm long with a diffractive grating with either 600 or 1800 lines per mm. This way, it is possible to perform measurements resolved in space, angle, and energy. An image of the real space is reconstructed before the CCD to apply a spatial filter by using a slit, enabling the selection of one or both gratings. The residual laser signal is suppressed with a long-pass spectral filter at 1.55 eV (≈800 nm). The time resolved images are performed in the same configuration, but directing the signal into a streak camera after passing the monochromator. The temporal reconstruction of the far field resolved in energy is made by moving vertically the focusing lens with a motorized station before it reaches the streak camera. Further details on the experimental setup and its schematic representation are presented in Supplement 1.

See Supplement 1 for supporting content.

REFERENCES

1. A. Kavokin, J. J. Baumberg, G. Malpuech, and F. P. Laussy, *Microcavities*, 2nd ed. (Oxford Science, 2008).
2. C. Weisbuch, M. Nishioka, A. Ishikawa, and Y. Arakawa, "Observation of the coupled exciton-photon mode splitting in a semiconductor quantum microcavity," Phys. Rev. Lett. **69**, 3314–3317 (1992).
3. J. J. Baumberg, P. G. Savvidis, R. M. Stevenson, A. I. Tartakovskii, M. S. Skolnick, D. M. Whittaker, and J. S. Roberts, "Parametric oscillation in a vertical microcavity: a polariton condensate or micro-optical parametric oscillation," Phys. Rev. B **62**, R16247 (2000).

4. A. Baas, J. Ph. Karr, M. Romanelli, A. Bramati, and E. Giacobino, "Optical bistability in semiconductor microcavities in the nondegenerate parametric oscillation regime: analogy with the optical parametric oscillator," Phys. Rev. B **70**, 161307 (2004).

5. J. Kasprzak, M. Richard, S. Kundermann, A. Baas, P. Jeambrun, J. M. J. Keeling, F. M. Marchetti, M. H. Szymańska, R. André, J. L. Staehli, V. Savona, P. B. Littlewood, B. Deveaud, and L. S. Dang, "Bose–Einstein condensation of exciton polaritons," Nature **443**, 409–414 (2006).

6. R. Balili, V. Hartwell, D. Snoke, L. Pfeiffer, and K. West, "Bose-Einstein condensation of microcavity polaritons in a trap," Science **316**, 1007–1010 (2007).

7. A. Amo, J. Lefrère, S. Pigeon, C. Adrados, C. Ciuti, I. Carusotto, R. Houdré, E. Giacobino, and A. Bramati, "Superfluidity of polaritons in semiconductor microcavities," Nat. Phys. **5**, 805–810 (2009).

8. G. Lerario, A. Fieramosca, F. Barachati, D. Ballarini, K. S. Daskalakis, L. Dominici, M. De Giorgi, S. A. Maier, G. Gigli, S. Kéna-Cohen, and D. Sanvitto, "Room-temperature superfluidity in a polariton condensate," Nat. Phys. **13**, 837–841 (2017).

9. K. G. Lagoudakis, M. Wouters, M. Richard, A. Baas, I. Carusotto, R. André, L. S. Dang, and B. Deveaud-Plédran, "Quantized vortices in an exciton–polariton condensate," Nat. Phys. **4**, 706–710 (2008).

10. D. Sanvitto and S. Kéna-Cohen, "The road towards polaritonic devices," Nat. Materials **15**, 1061–1073 (2016).

11. D. Ballarini, M. De Giorgi, E. Cancellieri, R. Houdré, E. Giacobino, R. Cingolani, A. Bramati, G. Gigli, and D. Sanvitto, "All-optical polariton transistor," Nat. Commun. **4**, 1778 (2013).

12. F. Marsault, H. S. Nguyen, D. Tanese, A. Lemaître, E. Galopin, I. Sagnes, A. Amo, and J. Bloch, "Realization of an all optical exciton-polariton router," Appl. Phys. Lett. **107**, 201115 (2015).

13. A. Imamoğlu, R. J. Ram, S. Pau, and Y. Yamamoto, "Nonequilibrium condensates and lasers without inversion: exciton-polariton lasers," Phys. Rev. A **53**, 4250 (1996).

14. D. Bajoni, P. Senellart, E. Wertz, I. Sagnes, A. Miard, A. Lemaître, and J. Bloch, "Polariton laser using single micropillar GaAs-GaAlAs semiconductor cavities," Phys. Rev. Lett. **100**, 047401 (2008).

15. T.-C. Chang, K.-B. Hong, S.-Y. Kuo, and T.-C. Lu, "Demonstration of polarization control GaN-based micro-cavity lasers using a rigid high-contrast grating reflector," Sci. Rep. **9**, 13055 (2019).

16. S. Christopoulos, G. Von Högersthal, A. J. D. Grundy, P. G. Lagoudakis, A. V. Kavokin, J. J. Baumberg, G. Christmann, R. Butté, E. Feltin, J. F. Carlin, and N. Grandjean, "Room-temperature polariton lasing in semiconductor microcavities," Phys. Rev. Lett. **98**, 126405 2007.

17. G. Christmann, R. Butté, E. Feltin, J.-F. Carlin, and N. Grandjean, "Room temperature polariton lasing in a GaN/AlGaN multiple quantum well microcavity," Appl. Phys. Lett. **93**, 051102 (2008).

18. S. Kéna-Cohen and S. R. Forrest, "Room-temperature polariton lasing in an organic single-crystal microcavity," Nat. Photonics **4**, 371–375 (2010).

19. K. S. Daskalakis, S. A. Maier, R. Murray, and S. Kéna-Cohen, "Nonlinear interactions in an organic polariton condensate," Nat. Mater. **13**, 271–278 (2014).

20. T. Guillet, M. Mexis, J. Levrat, G. Rossbach, C. Brimont, T. Bretagnon, B. Gil, R. Butté, N. Grandjean, L. Orosz, F. Réveret, J. Leymarie, J. Zúñiga Pérez, M. Leroux, F. Semond, and S. Bouchoule, "Polariton lasing in a hybrid bulk ZnO microcavity," Appl. Phys. Lett. **99**, 161104 (2011).

21. T.-C. Lu, Y.-Y. Lai, Y.-P. Lan, S.-W. Huang, J.-R. Chen, Y.-C. Wu, W.-F. Hsieh, and H. Deng, "Room temperature polariton lasing vs photon lasing in a ZnO-based hybrid microcavity," Opt. Express **20**, 5530–5537 (2012).

22. M. K. Seo, K. Y. Jeong, J. K. Yang, Y. H. Lee, H. G. Park, and S. B. Kim, "Low threshold current single-cell hexapole mode photonic crystal laser," Appl. Phys. Lett. **90**, 171122 (2007).

23. S. Azzini, D. Gerace, M. Galli, I. Sagnes, R. Braive, A. Lemaître, J. Bloch, and D. Bajoni, "Ultra-low threshold polariton lasing in photonic crystal cavities," Appl. Phys. Lett. **99**, 111106 (2011).

24. M. Nomura, N. Kumagai, S. Iwamoto, Y. Ota, and Y. Arakawa, "Photonic crystal nanocavity laser with single quantum dot gain," in Optics InfoBase Conference Papers (2009).

25. I. Rosenberg, Y. Mazuz-Harpaz, R. Rapaport, K. West, and L. Pfeiffer, "Electrically controlled mutual interactions of flying waveguide dipolaritons," Phys. Rev. B **93**, 195151 (2016).

26. P. M. Walker, L. Tinkler, M. Durska, D. M. Whittaker, I. J. Luxmoore, B. Royall, D. N. Krizhanovskii, M. S. Skolnick, I. Farrer, and D. A. Ritchie, "Exciton polaritons in semiconductor waveguides," Appl. Phys. Lett. **102**, 012109 (2013).

27. I. Rosenberg, D. Liran, Y. Mazuz-Harpaz, K. West, L. Pfeiffer, and R. Rapaport, "Strongly interacting dipolar-polaritons," Sci. Adv. **4**, eaat8880 (2018).

28. D. Liran, I. Rosenberg, K. West, L. Pfeiffer, and R. Rapaport, "Fully guided electrically controlled exciton polaritons," ACS Photon. **5**, 4249–4252 (2018).

29. P. Yu. Shapochkin, M. S. Lozhkin, I. A. Solovev, O. A. Lozhkina, Y. P. Efimov, S. A. Eliseev, V. A. Lovcjus, G. G. Kozlov, A. A. Pervishko, D. N. Krizhanovskii, P. M. Walker, I. A. Shelykh, M. S. Skolnick, and Y. V. Kapitonov, "Polarization-resolved strong light–matter coupling in planar GaAs/AlGaAs waveguides," Opt. Lett. **43**, 4526–4529 (2018).

30. M. W. Klein, T. Tritschler, M. Wegener, and S. Linden, "Lineshape of harmonic generation by metallic nanoparticles and metallic photonic crystal slabs," Phys. Rev. B **72**, 115113 (2005).

31. X. Zhang, S. Feng, J. Zhang, T. Zhai, H. Liu, and Z. Pang, "Sensors based on plasmonic-photonic coupling in metallic photonic crystals," Sensors **12**, 12082–12097 (2012).

32. D. A. Gollmer, C. Lorch, F. Schreiber, D. P. Kern, and M. Fleischer, "Enhancing light absorption in organic semiconductor thin films by one-dimensional gold nanowire gratings," Phys. Rev. Mater. **1**, 054602 (2017).

33. H. Stoll and A. Yariv, "Coupled-mode analysis of periodic dielectric waveguides," Opt. Commun. **8**, 5–8 (1973).

34. A. Yariv, "Coupled-mode theory for guided-wave optics," IEEE J. Quantum Electron. **9**, 919–933 (1973).

35. A. Yariv and P. Yeh, Photonics: Optical Electronics in Modern Communications (2007).

36. B. R. Bennett, R. A. Soref, and J. A. Del Alamo, "Carrier-induced change in refractive index of InP, GaAs and InGaAsP," IEEE J. Quantum Electron. **26**, 113–122 (1990).

37. W. Chow and D. Depatie, "Carrier-induced refractive-index change in quantum-well lasers," Opt. Lett. **13**, 303–305 (1988).

38. S. Murata, A. Tomita, and A. Suzuki, "Influence of free carrier plasma effect on carrier-induced refractive index change for quantum-well lasers," IEEE Photon. Technol. Lett. **5**, 16–19 (1993).

39. O. Svelto, Principles of Lasers, 5th ed. (Springer, 2010).

40. O. Jamadi, F. Reveret, P. Disseix, F. Medard, J. Leymarie, A. Moreau, D. Solnyshkov, C. Deparis, M. Leroux, E. Cambril, S. Bouchoule, J. Z. Pérez, and G. Malpuech, "Edge-emitting polariton laser and amplifier based on a ZnO waveguide," Light Sci. Appl. **7**, 82 (2018).

41. C. Grossmann, C. Coulson, G. Christmann, I. Farrer, H. E. Beere, D. A. Ritchie, and J. J. Baumberg, "Tuneable polaritonics at room temperature with strongly coupled Tamm plasmon polaritons in metal/air-gap microcavities," Appl. Phys. Lett. **98**, 231105 (2011).

42. A. Dreismann, H. Ohadi, Y. del Valle-Inclan Redondo, R. Balili, Y. G. Rubo, S. I. Tsintzos, G. Deligeorgis, Z. Hatzopoulos, P. G. Savvidis, and J. J. Baumberg, "A sub-femtojoule electrical spin-switch based on optically trapped polariton condensates," Nat. Mater. **15**, 1074–1078 (2016).

43. G. Christmann, C. Coulson, J. J. Baumberg, N. T. Pelekanos, Z. Hatzopoulos, S. I. Tsintzos, and P. G. Savvidis, "Control of polariton scattering in resonant-tunneling double-quantum-well semiconductor microcavities," Phys. Rev. B **82**, 113308 (2010).

44. H. Y. Kim, K. Lee, J. W. Lee, S. Kim, G. T. Kim, and G. S. Duesberg, "Electrical properties of high density arrays of silicon nanowire field effect transistors," J. Appl. Phys. **114**, 144503 (2013).